The Astrophysical Journal, 617:600–613, 2004 December 10

OBSERVATIONAL CONSEQUENCES OF A MAGNETIC FLUX ROPE EMERGING INTO THE CORONA

S. E. Gibson,[1] Y. Fan,[1] C. Mandrini,[2] G. Fisher,[3] and P. Demoulin[4]

Received 2004 April 9; accepted 2004 August 9

ABSTRACT

We show that a numerical simulation of a magnetic flux rope emerging into a coronal magnetic field predicts solar structures and dynamics consistent with observations. We first consider the structure, evolution, and relative location and orientation of S-shaped, or sigmoid, active regions and filaments. The basic assumptions are that (1) X-ray sigmoids appear at the regions of the flux rope known as "bald-patch–associated separatrix surfaces (BPSSs), where, under dynamic forcing, current sheets can form, leading to reconnection and localized heating, and that (2) filaments are regions of enhanced density contained within dips in the magnetic flux rope. We demonstrate that the shapes and relative orientations and locations of the BPSS and dipped field are consistent with observations of X-ray sigmoids and their associated filaments. Moreover, we show that current layers indeed form along the sigmoidal BPSS as the flux rope is driven by the kink instability. Finally, we consider how apparent horizontal motions of magnetic elements at the photosphere caused by the emerging flux rope might be interpreted. In particular, we show that local correlation tracking analysis of a time series of magnetograms for our simulation leads to an underestimate of the amount of magnetic helicity transported into the corona by the flux rope, largely because of undetectable twisting motions along the magnetic flux surfaces. Observations of rotating sunspots may provide better information about such rotational motions, and we show that if we consider the separated flux rope legs as proxies for fully formed sunspots, the amount of rotation that would be observed before the region becomes kink unstable would be in the range 40°–200° per leg/sunspot, consistent with observations.

Subject headings: MHD — Sun: corona — Sun: coronal mass ejections (CMEs) — Sun: magnetic fields

Online material: color figures, mpeg animations

1. BACKGROUND

Solar explosive events such as coronal mass ejections (CMEs) and flares are commonly considered to be driven by the free magnetic energy stored in current-carrying (twisted or sheared) coronal magnetic fields. Since little or no data are available on coronal magnetic fields, we rely on observations of coronal plasma for evidence of twisted magnetic field. It is not difficult to find apparently twisted or braided structures in the corona, both erupting and quiescent (Fig. 1), but we must be cautious in our interpretation of the magnetic fields associated with them. These observations are of three-dimensional structures projected onto the plane of the sky. Moreover, although plasma and field are frozen together in the highly conducting corona so that coronal structures may essentially trace the magnetic field, the plasma only becomes distinctly observable under certain density and temperature conditions dictated by an observing instrument. It is also useful to bear in mind that there must be a physical reason that the plasma tied to certain portions of the field has become visible. In order to deduce magnetic field structure from observed projections of plasma structures, we therefore require a three-dimensional, physical model that realistically simulates observable properties of the relationship between plasma and field.

The purpose of this paper is to consider the observable properties of a magnetic flux rope emerging into a coronal atmosphere, using the results of a numerical MHD simulation (Fan & Gibson 2003, 2004). Magnetic flux ropes are a particularly promising field topology used in models of CMEs and their precursors (Low 1994, 1996; Rust 1994). We define magnetic flux ropes as a set of magnetic field lines that collectively wind about a central, axial field line. Such a magnetic configuration has a plausible origin in the solar interior, where rising magnetic flux tubes require a minimum amount of twist in order to be able to rise cohesively through the convection zone (Emonet & Moreno-Insertis 1998; Fan et al. 1998; Abbett et al. 2000, 2001). It is also supported by photospheric observations (Tanaka 1991; Leka et al. 1996; Lites et al. 1995) that suggest the emergence of twisted flux ropes. When the magnetic flux rope configuration is incorporated into a fully MHD model, it explains observations of the so-called three-part structure of CMEs and their precursors, that is, white-light structures having a front, cavity, and core (Illing & Hundhausen 1986; Low & Hundhausen 1995; Chen 1996; Gibson & Low 1998, 2000; Guo & Wu 1998). Figure 2 shows observed examples of such structures, both for a quiescent (nonerupting) structure and for a CME. Since a well-defined cavity and core are visible prior to eruptions, the flux rope interpretation implies that ropes also exist in the corona prior to the eruption.

In the flux rope interpretation, the core of the CME is identified with the coronal prominence (or filament; we use the terms interchangeably in this paper). The bottoms of the windings of flux ropes provide natural dipped magnetic field configurations capable of supporting prominences. Observed properties including magnetic inverse configuration (where the field across the filament is opposite to that predicted by a potential field anchored to the photosphere below), apparently vertical filament "feet," and S-shaped filaments (Fig. 3) can be reproduced by flux rope models (Priest et al. 1989; Rust & Kumar 1994; Lites & Low 1997; Gibson & Low 1998; Aulanier & Demoulin 1998).

[1] High Altitude Observatory, National Center for Atmospheric Research, P.O. Box 3000, Boulder, CO 80307-3000.
[2] Instituto de Astronomía y Física del Espacio, IAFE, Casilla de Correos 67, Succursale 28, 1428 Buenos Aires, Argentina.
[3] Space Science Laboratories, Grizzly Peak at Centennial Drive, MC 7450, Berkeley, CA 94720-7450.
[4] Observatoire de Paris, LESIA, UMR 8109 (CNRS), F-92195 Meudon, France.

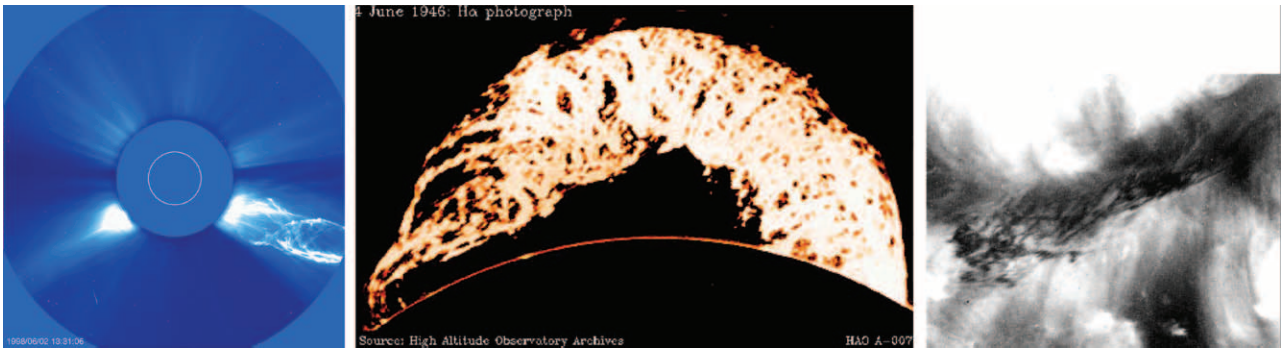

FIG. 1.—Coronal structures with apparent twist. *Left*: Crisscross structure of CME core (*SOHO* LASCO/C2 white light). *Middle*: Slinky-like "granddaddy" prominence viewed at the solar limb (HAO Hα). *Right*: Crisscross structure in *non*erupting filament viewed on the solar disk, 1998 August 14 (*TRACE* 195 Å absorption).

Magnetic flux rope models can also explain S-shaped hot coronal loops as seen in X-ray observations of so-called sigmoid active regions (Fig. 3) (Rust & Kumar 1994; Canfield et al. 2000). S-shaped magnetic field lines are natural products of any twisted or sheared field; in fact, field lines oriented both as forward and backward S's tend to arise (see, e.g., Fig. 4). It is not enough to point to a subset of the magnetic field lines having S shapes; a convincing comparison to observations needs to address the question, why is that particular part of the magnetic field heated? Reconnection and associated dissipative heating can occur in current sheets, which, according to Parker (1994), can form when two initially spatially separate flux systems come into contact along surfaces of magnetic tangential discontinuity during the dynamical evolution of a magnetized fluid. In particular, this can occur along separatrices between flux regions kept topologically distinct by their differing connection to the (assumed) rigid photosphere. (For discussion of a two-dimensional example, see Low & Wolfson 1988.) In a three-dimensional magnetic flux rope system, a separatrix surface is formed by the field lines that wind about the rope axis and tangentially graze the photosphere with magnetic field concave up, forming a so-called bald patch (Bungey et al. 1996) of dipped magnetic field along the polarity inversion line at the photosphere (Fig. 4). Under dynamic forcing of the rope, the field lines lying above and within this bald-patch–associated separatrix surface (BPSS hereafter) are free to expand upward relative to the shorter, arcade-type field below and external to it. Tangential discontinuities thus may form along this S-shaped BPSS, because the magnetic connectivity is discontinuous across it. This leads to current sheet formation and sigmoid brightenings (Titov & Demoulin 1999; Low & Berger 2003).

Finally, magnetic flux rope models also explain observations of shearing or rotating motions of magnetic elements at the photosphere. The emergence of a magnetic flux rope will initially manifest in photospheric magnetograms as a magnetic bipole and subsequent separation of its two poles; this coincides with the emergence of the mostly horizontal central portion of the flux rope. As this portion clears the photosphere and the vertical "legs" of the flux rope continue to emerge, the footpoints of magnetic field lines will rotate around the center of each leg. As discussed in Brown et al. (2003), this is one possible explanation of observed horizontal rotation of sunspots

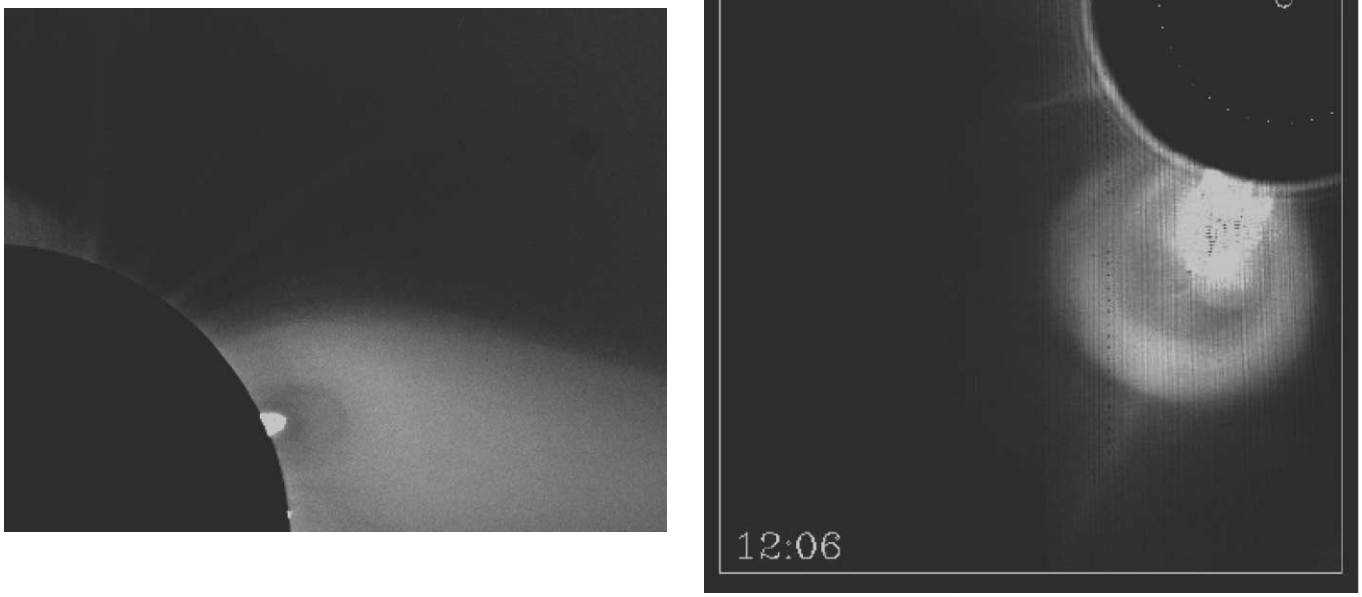

FIG. 2.—Three-part structure in white light containing cavity. *Left*: Quiescent prominence + cavity is seen in the 1998 March 18 Philippines eclipse image (NCAR/HAO Newkirk WLCC telescope). *Right*: Three-part CME in eruption on 1980 August 18 (HAO/SMM coronagraph).

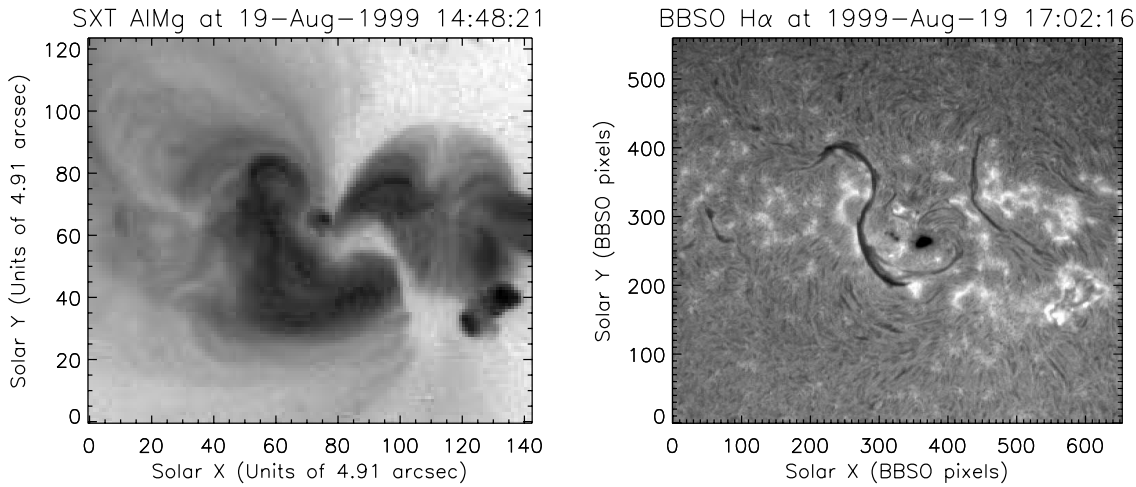

FIG. 3.—*Yohkoh* SXT X-ray (*left*; inverted color table) and BBSO Hα (*right*) observations of sigmoid active region NOAA 8668 and its associated filament on 1999 August 19 (from Gibson et al. 2002).

at the photosphere. The question of how to determine how much twist is brought into the corona using such observations of shearing and rotational motions at the photosphere is a nontrivial one, which we will consider in some detail below.

This paper will make use of the results of a numerical MHD simulation of a magnetic flux rope emerging into an overlying magnetic arcade (Fan & Gibson 2003, 2004). In § 2 we briefly summarize the aspects of those papers that are most relevant to the analysis presented here. In § 3 we discuss the location and evolution of the BPSS and its associated filament, and demonstrate that the BPSS is a region where current layers form during the eruption of the kink-unstable flux rope. In § 4 we consider the apparent motions of magnetic elements and how these might be interpreted in terms of the transfer of magnetic helicity into the corona. Finally, in § 5 we present our conclusions.

2. FLUX ROPE NUMERICAL MODEL

2.1. *Summary of Simulation Results*

The simulation of Fan & Gibson (2003, 2004) solves the MHD equations assuming an isothermal equation of state. The initial magnetic field in the corona is specified to be a potential bipolar arcade (Fig. 5, *red field lines*). For $t > 0$, the computational domain is driven at the lower boundary by a $\boldsymbol{v} \times \boldsymbol{B}$ electric field that corresponds to bodily lifting a twisted flux rope of prescribed form (see Fig. 1 of Fan & Gibson 2003) into the computational domain. The emerging flux rope is not initially force free: it is transported into the computational domain (corona) via the time-dependent electric field at the lower boundary and allowed to relax dynamically in the domain as governed by the isothermal MHD equations. Thus, although its transport across the photospheric boundary simulates a rigid flux rope entering the coronal domain, that rope can evolve in the corona and modify its initial form. The rope emergence is driven at a constant speed, and after $t = 54$ when the half-torus is fully transported, we stop the rise and anchor the field lines by setting the electric field at the lower boundary to zero. At the vicinity of the rope axis, field lines wind about the axis at a rate such that over the length of the fully emerged half-torus, each field line winds about the axis by about $1.875 \times 2\pi$.

Panels 1a–4a and 1b–4b of Figure 5 show the three-dimensional evolution of the coronal magnetic field, driven at

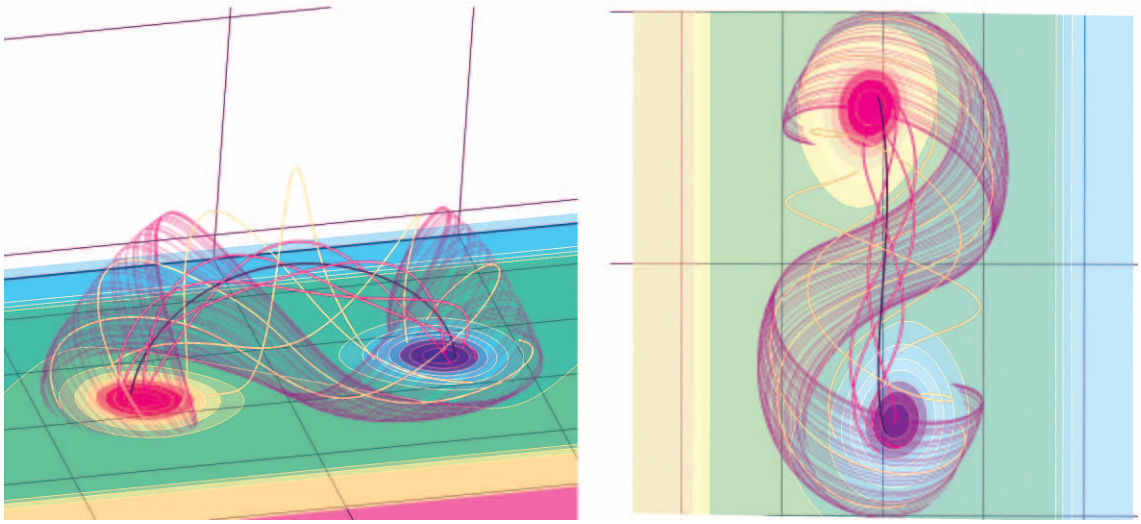

FIG. 4.—BPSS (*purple field lines*) overlaid on sample flux rope field lines for Fan & Gibson (2003, 2004) simulation time step 39. Color contours at lower boundary represent normal magnetic field at the photosphere. The BP is the locus of points where dipped field just touches the photosphere (i.e., at the centers of the purple field lines shown). The BPSS is made up of the field lines that contain the BP points.

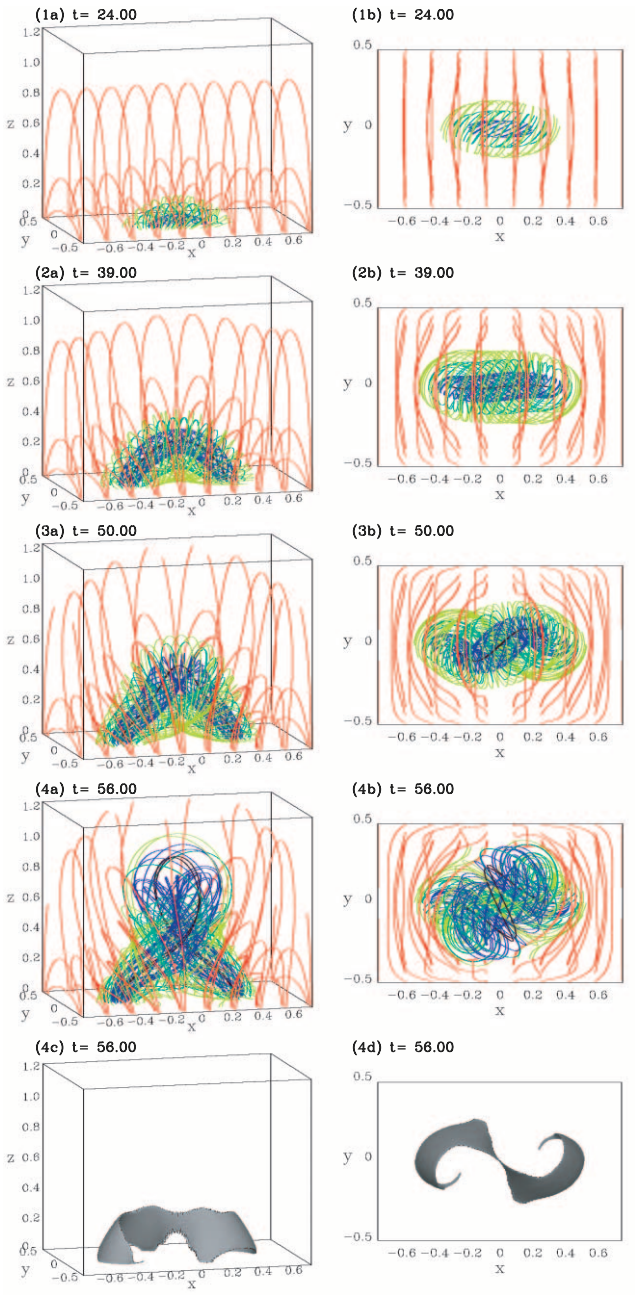

FIG. 5.—Panels 1a–4a and 1b–4b show the three-dimensional evolution of the coronal magnetic field, when driven at the lower boundary by the emergence of a twisted flux rope into an overlying coronal arcade (*red field lines*). Field lines in the rope are color-coded based on the flux surfaces of the initial tube they belong to. When the emerged rope became substantially kinked (panels 4a and 4b), a curved layer of highly concentrated current formed an inverse-S shape as viewed from the top (panels 4c and 4d). (From Fan & Gibson 2003.)

the lower boundary by the emergence of the twisted flux tube. The early evolution of the emerging magnetic field in the corona is nearly quasi-static because of the sub-Alfvénic speed with which the flux rope is transported through the lower boundary. At about $t \sim 45$, the amount of field-line twist as measured by the angle (Φ) of field-line rotation about the axis between the footpoints of the emerged tube has reached about $1.5 \times 2\pi$, and the rope undergoes the onset of a kink instability. We continue driving the flux tube emergence until $t = 54$, when Φ reaches $1.875 \times 2\pi$. The flux rope develops substantial writhing with an anticlockwise rotation at the apex of the rope axis reaching about 120° at $t = 56$ (see panels 4a and 4b of Fig. 5). Note that the writhing of the rope axis is left-handed, resulting in a forward-S shape for the upward-protruding rope axis as viewed from the top (see the black field lines in panels 3b and 4b of Fig. 5). The majority of active regions in the northern hemisphere show preferentially left-handed twist, the same sense as our emerging rope. However, the coronal X-ray sigmoids seen in the northern hemisphere have preferentially inverse-S morphology, opposite to the forward-S shape of our kinked rope axis. We therefore do not identify the kinked axis with the X-ray sigmoid. Instead, we consider the new curved layer of highly concentrated current that forms and becomes the dominant feature in the current distribution in the corona as the observed sigmoid; this layer appears as the twisted flux rope develops substantial writhing because of the kink instability. Panels 4c and 4d of Figure 5 show the three-dimensional isosurface of the electric current density $j = |\nabla \times \boldsymbol{B}|$ in the corona corresponding to the field shown in panels 4a and 4b at $t = 56$. As viewed from the top (see panel 4d of Fig. 5), the curved layer of current concentration shows an inverse-S shape, consistent with the morphology of X-ray sigmoids in the northern hemisphere.

2.2. *Relevance of Simulation to Coronal Field Emergence*

It is important to note that our kinematic representation of the emergence of the flux rope is an idealization of what we would expect to actually occur on the Sun and, for example, does not include the effect of gravity on the ability of the dipped field of the flux rope to cross the heavy photosphere. Fan (2001) showed in a simulation that described the dynamic evolution of a flux rope crossing the photospheric boundary that indeed the mass in the dips could weigh the flux rope down to the extent that it could not fully emerge into the corona. However, more recently Manchester et al. (2004) did a similar simulation using a shorter flux rope and found that in that case the mass drained more effectively and the upper part of the rope was able to lift off, disengaging the mass in the dips by reconnection. Even if such eventual "emergence" of the mass-loaded dips of the flux rope can occur, it is clear that dipped field crossing the photospheric boundary will behave differently than the nondipped arcade-like loops that emerge with the top of the flux rope. Thus our rigid and smooth translation of the flux rope across the photospheric boundary is an oversimplification. The real rope is more likely to emerge/reform in the atmosphere in fits and starts. However, if these fits and starts are very fast compared to our sub-Alfvénic emergence speed, then our idealized, smooth emergence is at least qualitatively equivalent to the more complex process of emergence that may occur in the actual Sun. It is worth pointing out that one effect of a dynamic emergence that is not captured by our simulation would be heating along current sheets at the boundary between mass-loaded dipped field and dipped field that has lifted off once it has unloaded its mass via reconnection. This quiescent heating may be at least partly responsible for the long-lived, noneruptive X-ray sigmoids, further discussed below.

An alternative to the full bodily emergence of a twisted magnetic flux rope across the photosphere has been suggested by Longcope & Welsch (2000). In their model, not all of the twist of the subphotospheric flux tube crosses the photosphere with the magnetic flux of the flux rope. However, with time, a magnetic torque arises from the twisted field trapped subphotospherically. Since this torque cannot be compensated by plasma forces, after a transient period it drives photospheric flows (components of a torsional Alfvén wave) that transport helicity into the coronal field. Pevtsov et al. (2003) predicted the development

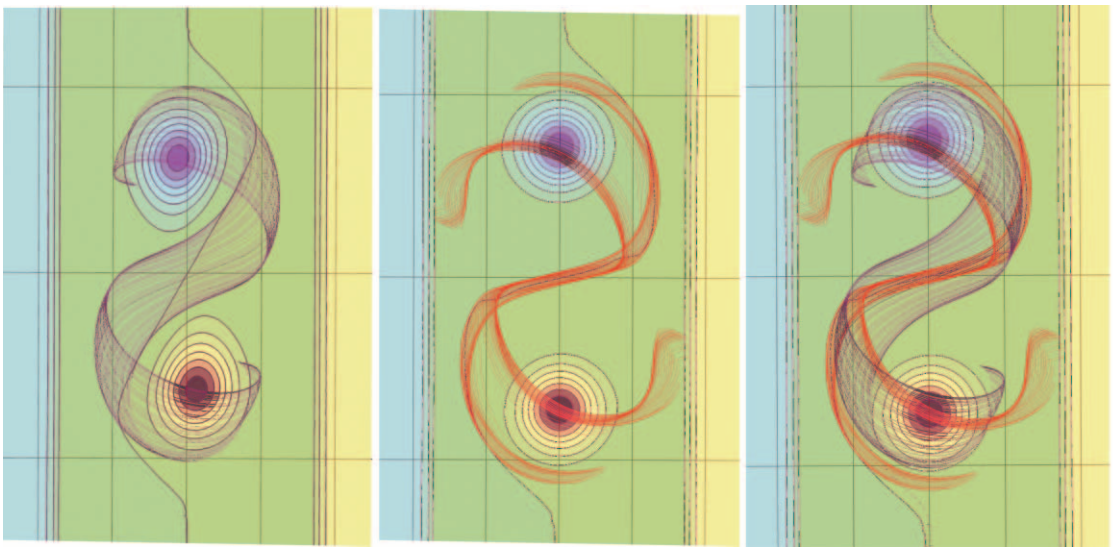

FIG. 6.—BPSSs for time steps 39 (*left*; *purple lines*), 56 (*middle*; *red lines*), and an overlay of both (*right*). These two BPSSs represent completely different sets of field lines within the emerging flux rope, and not the time evolution of one fixed set. Color contours at lower boundary represent the normal component of the magnetic field at the photosphere. The photospheric polarity inversion line is shown in purple. [*This figure is available as an mpeg file in the electronic edition of the Journal.*]

of twist via this mechanism to have a timescale of roughly 1 day, and found reasonable agreement between model predictions and observations of a set of active regions. This mechanism is physically very different than that of an actually emerging flux rope. However, again it is qualitatively equivalent to the kinematic "emergence" of a flux rope that we are describing in this paper, which describes the formation of a coronal rope with ever-increasing flux and twist. Whether this twist is carried into the corona with the flux of the rope, or whether it is transported over time via photospheric motions (Amari et al. 1996; Tokman & Bellan 2002; Torok & Kliem 2003), the net quasi-static evolution of the rope in the corona and apparent motions at the photosphere would be quite similar.

3. SIGMOID FEATURES: OBSERVATION VERSUS FLUX ROPE TOPOLOGY

3.1. *From BPSS to Current Sheets to X-Ray Sigmoids*

The simulation of Fan & Gibson (2003, 2004) thus provides one good physical explanation for X-ray sigmoids: it is reasonable to predict heating to X-ray temperatures along the current layers that form during the kink instability–driven eruption. In this paper, however, we wish to probe one level deeper and consider why the current layers form in the location and shape that they do. By arguing that it is due to the basic topology of a flux rope partly line-tied to a rigid photosphere, we support the theory that sigmoids arise under far more general conditions than that of our simulation. In other words, the kink instability is just one dynamic driver that could cause current sheet formation along the crucial separatrix surface.

Previous analytic models have shown that the BPSS for a flux rope partially emerged through a rigid photosphere will be sigmoid shaped and will have the correct direction of S for the sign of helicity of the rope (Titov & Demoulin 1999; Low & Berger 2003). The left panel of Figure 6 shows the BPSS for the numerical simulation at time step 39, before the rope axis has become kinked. Although no significant current layers have formed, the inverse-S shaped BPSS is already there. The middle panel of Figure 6 shows the BPSS for time step 56, when the rope is greatly kinked, and the right panel shows the overlay of the BPSSs for $t = 39$ and $t = 56$. A movie of the time evolution of the BPSS is available as an mpeg file in the electronic edition of the Journal. It is important to realize that the evolving BPSS shown in this movie and in the two time steps of Figure 6 is made up of different field lines for each time step. That is, the BPSS is the set of all field lines that intersect the photospheric BP (the central portion of the photospheric polarity inversion line), and this BP evolves in a manner consistent with the continued emergence of a flux rope. As the rope emerges, the dipped field that used to be the BP moves up and away from the photosphere, to be replaced by dipped field from lower down in the emerging flux rope. In our simulation, this slow emergence does not drive the formation of a current sheet along the BPSS, as it might in the dynamic Sun, since on the timescale of emergence the BPSS is not a topological feature separating field lines with independent connectivity (i.e., field lines above and below the BPSS are evolving in an equivalent way during emergence, since the dipped lines are allowed to enter the computational domain). Thus, prior to the kink instability onset, the BPSS evolves primarily by extending and becoming more S-shaped as the amount of twist in the corona increases.

However, when the kink instability sets in, an internal evolution of the system (i.e., not forced by the evolution at the boundary) starts on a very short timescale (a few Alfvén times). The evolution of the boundary is slow compared to this short timescale, so that the BPSS starts to have a topological meaning; it separates winding field lines above it from two arcade-like systems of field lines below. At this point the BPSS begins to undergo a significant change. In Figure 6 the field lines for both $t = 39$ and $t = 56$ intersect the BPs at 50 evenly spaced points, but as they extend up into the corona the $t = 56$ field lines diverge from the centers of the outer portions of the separatrix surface (the two ends of the inverse S). We need to clarify that the distribution of field lines in the BPSS is still continuous (that is, there are field lines along the BPSS within the gapped region at $t = 56$ that we have not drawn; it is just that field line density is low there). There are two plausible contributing reasons for this splitting of field lines.

The first effect is the ideal MHD process of current sheet formation. As the flux rope expands upward and pushes up

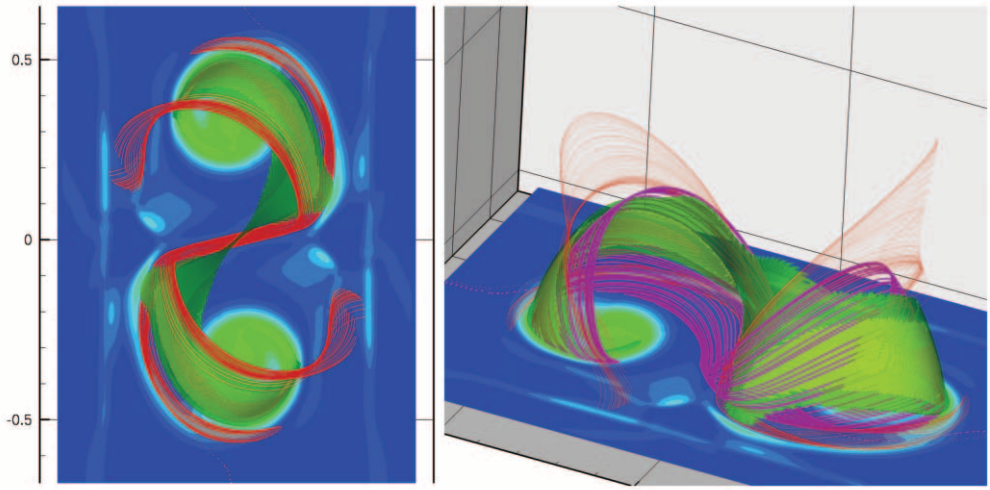

FIG. 7.—*Left*: Comparison of $t = 56$ BPSS (*red field lines*) to current sheets (*yellowish-green isosurfaces*). *Right*: Same, with $t = 39$ BPSS also shown (*purple field lines*). Color contours at bottom boundary represent magnitude of current at photosphere (same color scaling as coronal isosurfaces).

against the external, line-tied arcade field, the layers on each side of the BPSS that lie in between the two magnetic flux systems (rope and arcade) are squeezed. The magnetized fluid in these layers is expelled outward from the central, most squeezed parts. This is demonstrated in the time evolution movie beginning at $t = 50$ as a bifurcation of field lines away from the central portions of the two sides of the BPSS. Such a bifurcation of field lines implies the presence of a current sheet (Yu 1973; Parker 1994), and indeed, Figure 7 demonstrates this by overlaying the isosurfaces of the current layer found by Fan & Gibson (2003, 2004) with the BPSS of $t = 56$ (*left*) and with those of both $t = 39$ and $t = 56$ (*right*). The most intense current sheets (*yellowish-green isosurfaces*) have formed at the centers of the two ends of the inverse-S where the separatrix surface field lines have bifurcated.

The second plausible contributing factor to field line bifurcation arises from the resistive evolution of the system subsequent to current sheet formation. Reconnections are enabled with the important potential consequence of magnetic topology change. Field line bifurcation can then be enhanced as the footpoints of the two, increasingly split sets of field lines evolve in a qualitatively different manner. In the early stages of the field line bifurcation, as evidenced by $t = 52$ in the time evolution movie, the field lines of the BPSS still have both footpoints rooted in the bipolar field region associated with the emerging flux rope. Note that each field line has a low-lying portion and a high-lying portion, so that the bifurcations are between the high-lying portion of one set of field lines and the low-lying portion of the other set of field lines. By $t = 56$, as seen in Figure 6 and in the movie, the footpoints on the ends of the low-lying portions are still rooted in the bipolar region associated with the flux rope, but the footpoints on the ends of the high-lying portions of the field lines are now rooted in the external, arcade magnetic field. Since there are no photospheric velocities after $t = 54$, the only way these field lines can move footpoints so drastically is via magnetic reconnection. This reconnection has effectively mixed the two originally distinct flux systems.

The current layer is most intense in the two gaps of this final BPSS, but a significant layer extends along the entire S shape of the original, prekink BPSS. This current layer formation is analogous to the current sheets predicted along the separatrix line in the two-dimensional system of Low & Wolfson (1988; see Fig. 3 of that paper). In both that two-dimensional system and in our three-dimensional system, a dynamic forcing leads to distinct evolution of neighboring dipped versus arcade field lines due to their very different lengths, and a current layer forms along the interface between these flux systems. A less intense portion of the current layer extends vertically above the BP inversion line, along the center of the inverse S (see Fig. 7). This vertical current layer arises because as the flux rope erupts, the vacuum of field behind it must be filled in a manner consistent with the rigid lower boundary field, which effectively causes the flux rope legs to squeeze together. The current layer that forms between these tangentially discontinuous legs has its two-dimensional analog as discussed in Low (1987; see Fig. 6 of that paper or Fig. 2 of Low & Wolfson 1988). Recent work studying the stability of the Titov & Demoulin (1999) model to the kink instability has also demonstrated that a vertical current layer develops beneath the rising flux rope loop apex (Torok et al. 2004; Kliem et al. 2004). The vertical current layer in that analysis forms due to pinching along a magnetic X line, which, in the presence of a toroidal field, becomes a hyperbolic flux tube (HFT) where extremely diverging field lines are present (see Fig. 1 of Roussev et al. 2003 for a nice representation of the X line, and Titov et al. 2003 for a discussion of current sheets and HFTs). The vertical current sheet in our simulation is created by the squeezing together of the flux rope legs, while the X line location of the vertical current sheet of the Torok et al. (2004) simulation is in a sense a squeezing together of the overlying arcade field beneath the rising flux rope. However, both may be root causes of the large-scale vertical current sheet that forms below erupting flux in the standard model of the main phase of eruptive flares (Shibata 1999), which permits a detachment of some or all of the flux rope as reconnection closes the field behind it (see Kliem et al. 2004 for further discussion). Whether such a detachment could occur in our simulation, and whether a postflare end state, similar to the one in eruptive flares, would be achieved, is an interesting question and the subject of future work.

3.2. *BPSS and Dips: X-Ray Sigmoid versus Filament*

Pevtsov (2002b) found that 91% (124 out of 136 regions observed) of sigmoid active regions had a filament associated

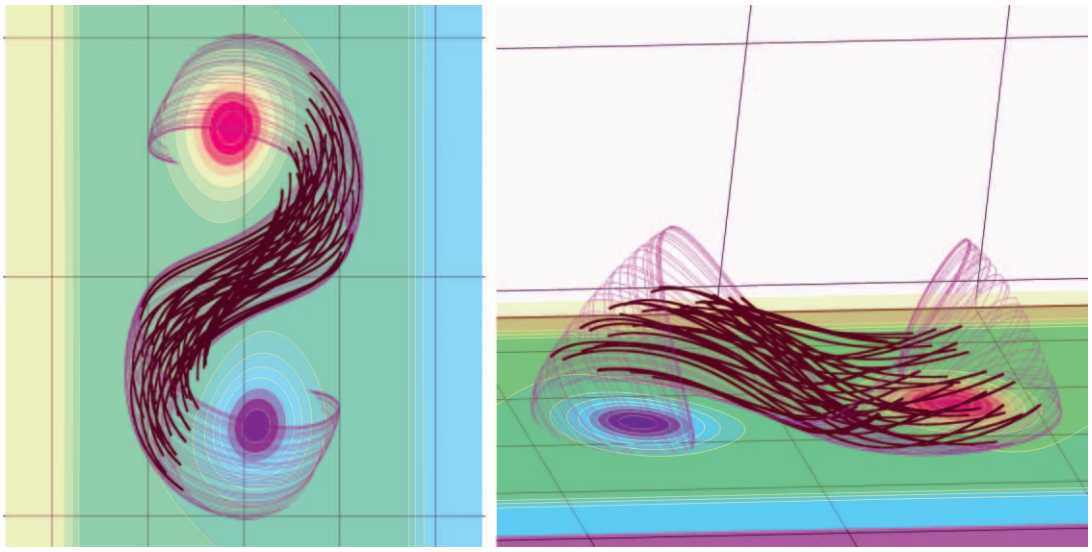

FIG. 8.—Two views of $t = 39$ BPSS (*purple field lines*) and dipped field representing filament (*brown*; note that the dipped field has been filled from the dip bottom up a distance $0.1L$ or to where the field direction becomes horizontal, whichever comes first; L is the shorter of the horizontal lengths of the simulation domain). Color contours at lower boundary represent normal component of the magnetic field at the photosphere.

with them. For the flux rope model, this is to be expected: the bottoms of the winding flux rope are dipped magnetic field where dense filaments can be supported (Priest et al. 1989). Figure 8 shows the locus of dipped field suspended in the corona that we identify as a potential location for filament material (indicated by brown points). Filament channels often exist without filaments, and not all of this region would necessarily be filled with plasma; however, the basic S-shaped structure that a filament might take on is clear, and it has the same direction of S shape as the associated BPSS. The filament lies within and above the BPSS, with the entire filament body nearly parallel to the photospheric polarity inversion line. In contrast, although the middle of the BPSS lies along the polarity inversion line, its footpoints are anchored in the opposite polarity fields. This is consistent with observed relationships between X-ray sigmoids and filaments (Pevtsov 2002a). Figure 8 can also be directly compared to Figure 3 to demonstrate how BPSS/dipped field capture the basic properties of X-ray sigmoid/sigmoidal filament.

The filament of necessity lies above the BPSS, and this raises the question of how, in some cases, X-ray sigmoids appear to erupt while their associated filaments remain unaffected (Pevtsov 2002b). To answer this, we must first clarify what is meant by the "eruption" of X-ray sigmoids. Sigmoid brightenings are, in our interpretation, a heating along current sheets that form at the BPSS during dynamic—but not necessarily eruptive—forcing. Thus it is plausible that the BPSS could be lit up in a quiescent manner when driven to reconnection, while the overlying filament remains thermally isolated and unperturbed. This noneruptive type of sigmoid brightening is commonly observed and is the case shown in the observations of Figure 3. Such long-lived, quiescent sigmoids often do eventually erupt, and by this we mean that they flare in clear conjunction with one or more eruptive signatures such as white-light CMEs, EUV and X-ray dimmings, postflare loops, or two ribbon flares. Even with clear indications of eruption, associated filaments are sometimes unaffected. It is plausible that in such cases a portion of the flux rope has erupted, with reconnection above the filament (see Gilbert et al. 2001). Note that in our simulation dipped field anchored at the photosphere, i.e., the BP, exists throughout; if reconnection occurs in the vertical current sheet above this, it is possible (but remains to be demonstrated) that a new equilibrium will arise in which some of the flux rope has erupted, while some, including dipped field that may still contain filament material, remains.

The fine structure within a filament can also be understood in terms of the flux rope model. When viewed on the disk the modeled filament has the overall structure of an inverse-S shape that is oriented at only a very small angle to the underlying neutral line; this is consistent with observations such as the Hα filament of Figure 3 (*right*). If coronal conditions are such that substructures within the region of dipped field become distinctly visible, the flux rope model implies that the filament would appear to have a crisscrossed structure. This is indeed the case of the high-resolution observations seen in the *TRACE* 195 Å observations of a quiescent filament (Fig. 1, *right*). Figure 9 shows the filament alone, viewed as if it were at the limb, both along the rope axis (*left*) and perpendicular to the rope axis (*right*). Again, if structure within the filament is resolved, both views demonstrate the sort of braided, crisscrossed structure seen in some white-light CME cores (e.g., Fig. 1, *left*). Note that the structures in the view parallel to the rope axis exhibit U shapes; such U-shaped fine structure observed in white-light CMEs have been used to argue for a flux rope axis oriented along the line of sight (Chen 1996; Wood et al. 1999). However, caution should be exercised because the structure seen in the view oriented perpendicular to the rope axis also exhibits broad concave-up features, and particularly if the filament (or equivalently, the CME core) mass is seen in a less fibril state, the general core appearance for the orientation perpendicular to the line of sight is also U shaped (Gibson & Low 2000). Indeed, Cremades & Bothmer (2004) did a survey of white-light CME structure in comparison to underlying neutral line orientation and found U-shaped structures for both orientations (see Fig. 9). We therefore feel that using observed white-light U shapes to determine orientation of a flux rope CME model requires caution; a much better technique is that utilized by Cremades & Bothmer (2004), who found that the broadness of a CME core relative to its surrounding cavity was

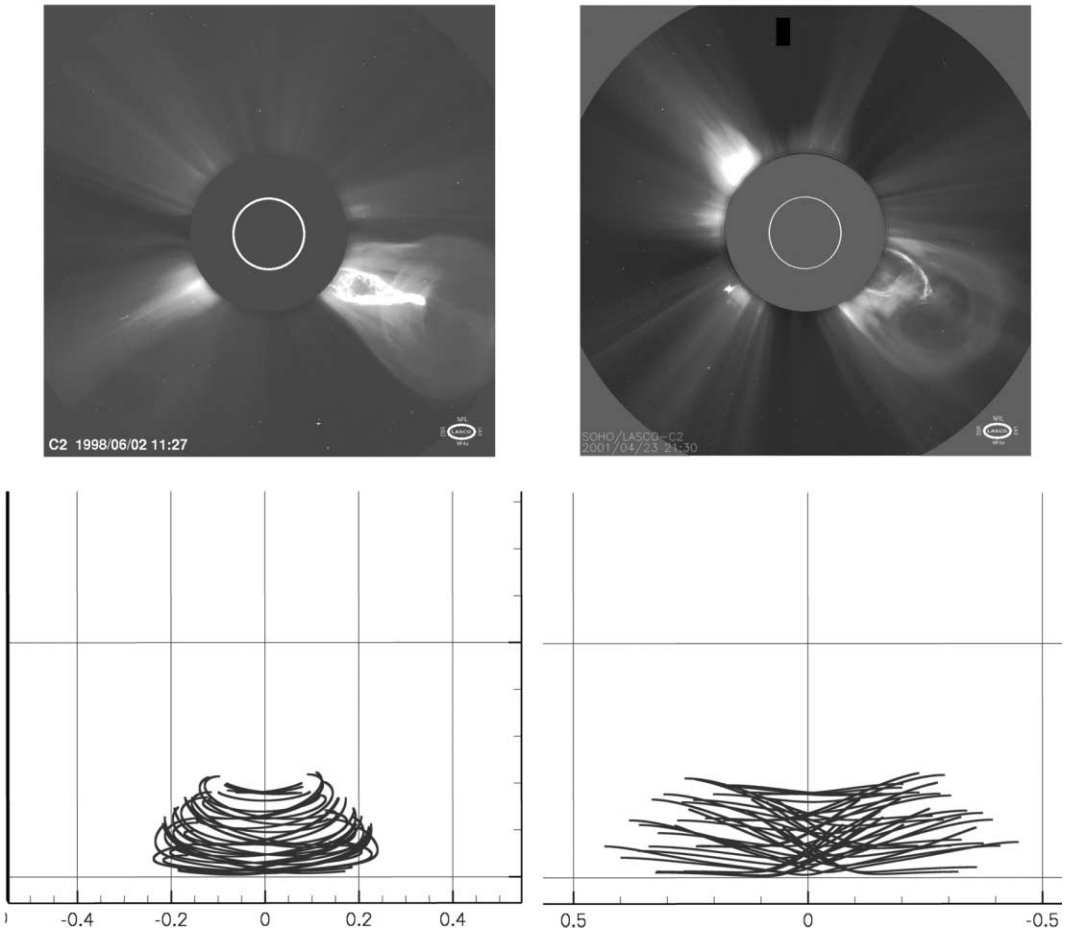

FIG. 9.—Two views, as at the solar limb, of $t = 39$ dipped field representing filament (*brown*) and white-light (*SOHO* LASCO/C2) CMEs exhibiting U-shaped fine structure whose orientation was determined from their underlying magnetic neutral lines (Cremades & Bothmer 2004). *Left*: View parallel to flux rope axis/underlying neutral line. *Right*: View perpendicular to flux rope axis/underlying neutral line. [*See the electronic edition of the Journal for a color version of this figure.*]

a good indicator of the orientation of the underlying magnetic neutral line.

4. OBSERVATIONAL INTERPRETATIONS OF MAGNETIC ELEMENT MOTIONS

4.1. *Magnetic Helicity*

Magnetic helicity is of interest to studies of coronal dynamics because the twisting or shearing of magnetic fields is generally believed to be the primary energetic driver behind flares and CMEs. Magnetic helicity as a global quantity is very nearly conserved in a low-resistivity plasma such as the corona, and a well-defined, gauge-invariant relative helicity H integrated over our simulation volume can be calculated as a function of time. The amount of helicity injected through the lower boundary (i.e., photosphere) can also be determined, using the expression derived by Berger & Field (1984):

$$\frac{dH}{dt} = -2 \int \int [(\boldsymbol{A}_p \cdot \boldsymbol{v}_t) B_n - (\boldsymbol{A}_p \cdot \boldsymbol{B}_t) v_n] \, dx \, dy. \qquad (1)$$

In this expression, t and n stand for the vector components tangential to and normal to the photosphere, and $\boldsymbol{A}_p$ is the vector potential for the reference potential field having the same normal flux distribution as the magnetic field $\boldsymbol{B}$ at the photosphere and can be calculated directly from that boundary field. Because the only velocity in the simulation is the upward motion of the emerging tube, v_n, only the second term is nonzero. Fan & Gibson (2004) compared $H(t)$ of the flux rope as directly calculated via the volume integral to that expected due to injection by integration of dH/dt over time and found that they are nearly identical, as would be expected by helicity conservation, until late in the simulation ($t = 54$) when reconnections begin to break down the boundary between flux rope and arcade.

The calculations done in Fan & Gibson (2004) were enabled by the full knowledge of the vector magnetic field and velocity. However, Demoulin & Berger (2003) demonstrated that knowledge of the apparent horizontal velocity of magnetic elements at the photosphere, along with the normal magnetic field, is enough in principal to determine dH/dt. Specifically, they showed that the apparent horizontal velocity of the photospheric footpoints of magnetic field lines, $\boldsymbol{u}$, could be related to the tangential and normal components of the plasma velocity and magnetic field:

$$\boldsymbol{u} = \boldsymbol{v}_t - \frac{v_n}{B_n} \boldsymbol{B}_t. \qquad (2)$$

Thus the apparent horizontal velocity $\boldsymbol{u}$ is the sum of both "true" horizontal motions v_t as well as apparent horizontal

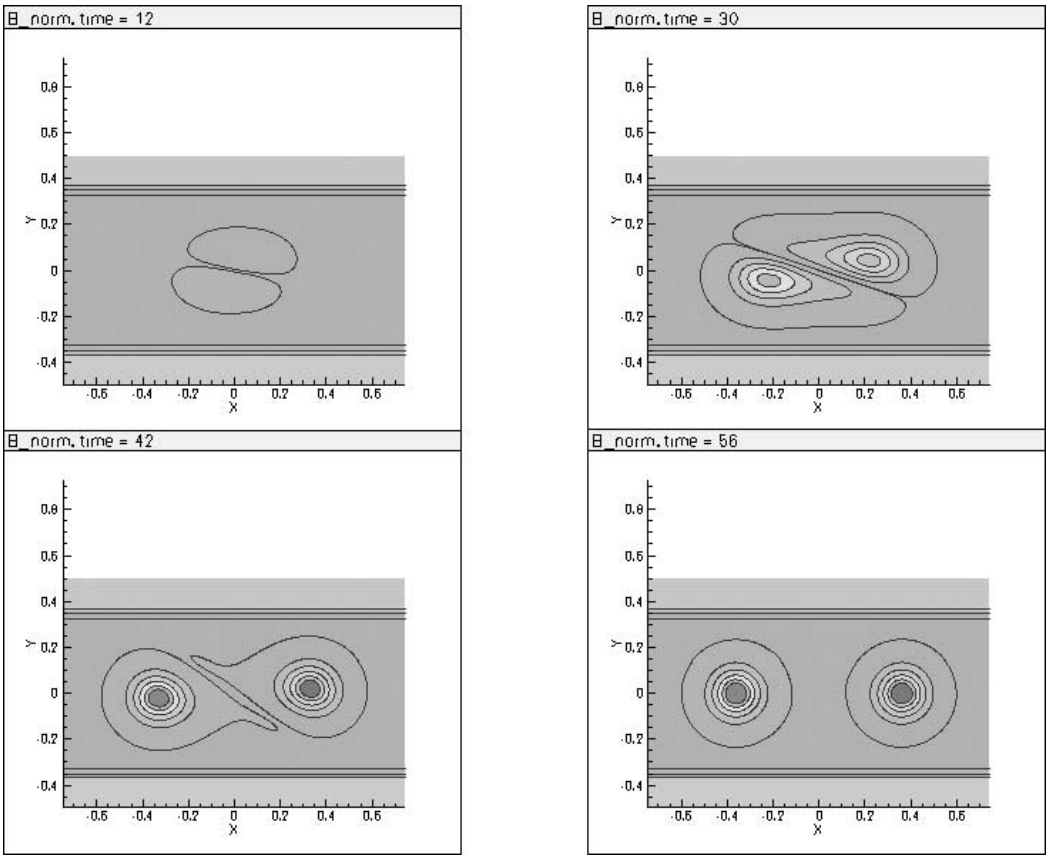

FIG. 10.—Evolution of the normal magnetic field at the photosphere for times $t = 12, 30, 42, 56$. [*See the electronic edition of the Journal for a color version and an mpeg animation of this figure.*]

motions due to the geometric effect of the emergence of the rope. From equations (1) and (2) it follows that

$$\frac{dH}{dt} = -2 \int \int (\boldsymbol{A}_p \cdot \boldsymbol{u}) B_n \, dx \, dy. \tag{3}$$

Therefore, since A_p can be calculated from B_n, dH/dt can be calculated from observations of the normal magnetic field and observed motions of magnetic elements.

4.2. *Evolution of the Normal Magnetic Field*

The evolution of the distribution of the normal field (B_n) for our emerging twisted flux rope is more complex than the simple separation of two separating magnetic polarities that occurs when an untwisted flux tube, forming an Ω loop, emerges. Figure 10 shows slices of the normal magnetic field at the lower boundary versus time, and the movie available as an mpeg file in the electronic edition of the Journal shows the full time evolution of the normal field. As the top part of the twisted magnetic flux tube crosses the lower boundary, a bipolar magnetic region grows, as characterized by two separating magnetic polarities of B_n ($t = 8$–20). At these early times of emergence, the axial magnetic component of the flux tube is mostly horizontal and so it has only a small contribution to the normal field distribution (B_n); the most important contribution of the B_n distribution rather comes from the azimuthal component (associated with the twist). This initial phase corresponds to the emergence of sheared magnetic arcades. The contribution of the azimuthal component to B_n forms two evolving elongations of the classical separating polarities, called magnetic "tongues" by Lopez Fuentes et al. (2000) ($t = 21$–31). The contribution of the azimuthal component of the field to B_n decreases as the central, horizontal portion of the flux rope fully emerges, and so these magnetic tongues are similarly diminished and ultimately disappear ($t = 33$–51). At this stage the normal magnetic field distribution resolves into two circular opposing polarities and does not change significantly as the two "legs" of the rope continue to emerge through the lower boundary ($t = 51$–54).

The evolution of magnetic tongues as demonstrated by our simulation is interesting for several reasons. First and foremost, such tongue evolution has been observed in the evolution of several active regions (Lopez Fuentes et al. 2000; Green et al. 2002; Mandrini et al. 2004) and arguably provides an observable means of distinguishing the emergence of a twisted flux rope from that of an untwisted Ω loop. Moreover, the orientation of the tongues is directly related to the sign of the twist of the emerging flux tube, so it provides a further means of determining the sign of the magnetic helicity simply from a longitudinal magnetogram. Finally, it is a reasonably model-independent observable: tongue evolution is expected for almost any twist distribution of an emerging flux rope; the difference between different twist profiles will simply affect the visibility of the tongues.

4.3. *Local Correlation Tracking Using Magnetograms*

One technique for determining the apparent horizontal velocity $\boldsymbol{u}$ is to apply local correlation tracking (LCT) to a time series of magnetograms of the photospheric normal field (November

& Simon 1988; Berger et al. 1998; Chae et al. 2001; Li et al. 2004). Classical LCT determines only the transverse velocities of magnetic features by determining their relative displacement between sequential magnetograms. In general, the full vector velocity would be of interest, particularly as an observational driver for simulations of evolving coronal active regions, which require a specification of $\boldsymbol{v} \times \boldsymbol{B}$ at the lower boundary, just as our idealized flux rope simulation does. Methods for determining the vector velocity include a correction to the LCT method that ensures that the vertical component of the induction equation is satisfied (Welsch et al. 2004; see also Kusano et al. 2002) and a method that uses an additional constraint minimizing kinetic energy in the system in order to find a vector velocity that explicitly satisfies the induction equation (Longcope 2004). However, both of these techniques can only provide information about the components of the vector velocity perpendicular to the local magnetic field. This is a consequence of the essentially underdetermined problem: flow parallel to $\boldsymbol{B}$ does not affect the induction equation. Ideally, it could be remedied by additional observations of plasma motions.

For our purposes the apparent horizontal velocity is enough to calculate helicity, so a classical LCT program is appropriate. We apply an LCT code (defined in Welsch et al. 2004 as "FLCT" for Fourier local correlation tracking to distinguish it from the induction equation–constrained ILCT method referred to above) to a time series of our simulation boundary field B_n and calculate $\boldsymbol{u}_{\rm LCT}$. We use an apodizing window, chosen to be smaller in size than the features that the technique is tracking, of $\sigma = 30$ pixels $= 0.1875L$, where L is the smaller of the two horizontal lengths of the simulation domain. From B_n and $\boldsymbol{u}_{\rm LCT}$ we then calculate $dH_{\rm LCT}/dt$. We also calculate $dH_{\rm exact}/dt$ using equation (1), and, in the same manner as Fan & Gibson (2004), integrate both $dH_{\rm LCT}/dt$ and $dH_{\rm exact}/dt$ in time to get the total magnetic helicity as a function of time. These helicities are expressed in units of ϕ^2, where ϕ is the total flux in the twisted flux tube. Figure 11 compares $H_{\rm exact}(t)$ (*solid line*) and $H_{\rm LCT}(t)$ (*triangles*).

As Figure 11 demonstrates, the LCT technique yields a helicity that is over an order of magnitude too small by the end of the rope evolution. The reason for this is clear from Figure 12, which compares $\boldsymbol{u}_{\rm LCT}$, which was calculated using LCT, to $\boldsymbol{u}_{\rm exact}$, which is calculated directly from equation (2). From this it is clear that although the LCT is catching the general lateral motion of the separating magnetic bipole, it is missing most of the rotational motion. The $t = 50$ panels show this very well: the actual field line footpoint motion $\boldsymbol{u}_{\rm exact}$ is vortical, but $\boldsymbol{u}_{\rm LCT}$ shows only a horizontal motion separating the magnetic poles of the flux rope. Note that the velocity vector lengths in Figure 12 are uniform, in order to demonstrate how the direction of velocity differs between $\boldsymbol{u}_{\rm exact}$ and $\boldsymbol{u}_{\rm LCT}$. Demoulin & Berger (2003) referred to such vortical motions as "undetectable" because they are motions that have no effect on the time evolution of the B_n distribution. The general case of such motions is $B_n\boldsymbol{u} = \nabla \mathsf{U} \times \boldsymbol{n}$, where U is an arbitrary function. Such motions are present in various forms throughout the evolution of our rope, but the motion primarily along the isocontours of B_n during the latter part of the rope evolution is a particularly intuitive example. Figure 13, which does scale the vector lengths with velocity magnitude, shows that much of the fastest $\boldsymbol{u}_{\rm exact}$ is due to exactly this sort of motion and is missed in $\boldsymbol{u}_{\rm LCT}$, so it is not surprising that $H_{\rm LCT}$ is grossly underestimated. A movie of the evolution of $\boldsymbol{u}_{\rm LCT}$ and $\boldsymbol{u}_{\rm exact}$ is available as an mpeg file in the electronic edition of the Journal.

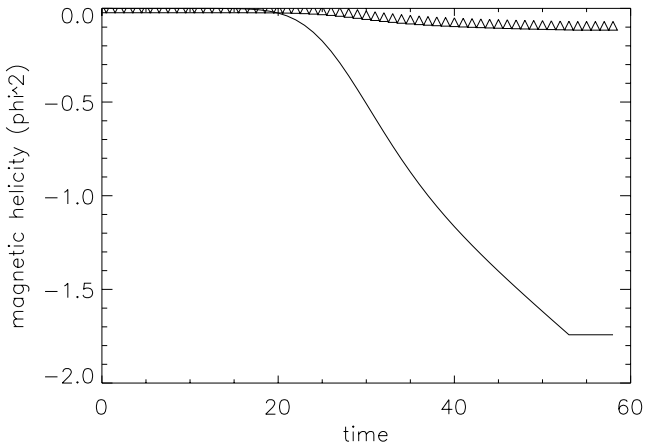

FIG. 11.—Total helicity injected through the photosphere as a function of time, as calculated exactly using known vertical velocity of the simulated flux rope emergence in combination with the normal magnetic field [$H_{\rm exact}(t)$; *solid line*], and as calculated using LCT of a time series of the normal magnetic field to establish an apparent horizontal velocity of magnetic elements [$H_{\rm LCT}(t)$; *triangles*]. Helicities are normalized to the total flux in the twisted flux tube.

4.4. *Rotating Sunspots*

The problem with $u_{\rm LCT}$ is that it is not showing all of the horizontal motion of magnetic field line footpoints, because the normal flux magnetograms do not show the footpoint motion along the smooth B_n isocontours of the simulated flux rope. In the real Sun, magnetic flux is highly fragmented (Strous et al. 1996; Berger et al. 1998; Strous & Zwaan 1999), and, for example, rotational motion of sunspots has long been observed. Recent studies have focused on high-resolution *TRACE* white-light observations, which show sunspot rotation particularly well (Nightingale et al. 2002; Brown et al. 2003).

Brown et al. (2003) studied seven sunspots using *TRACE* white-light time-slice data to determine average rotation profiles with respect to time, radius, and angle. The total rotation of each sunspot varied from between 40°–200°. The duration of rotation ranged from 3 to 5 days. Six of the seven spots studied had flares and/or CMEs that occurred during the observed time period, but only three of these eruptions were clearly related to the sunspot rotation. Two of the sunspots had sigmoids associated with them, and one had a flare with a distinctively "Slinky"-like appearance. There seemed to be a trend toward counterclockwise rotation in the northern hemisphere.

Our simulation of the emerging flux rope provides one possible explanation for such sunspot rotation. If we identify the sunspots with the legs of the flux rope, their rotation corresponds to the apparent vortical motion we observe around the two photospheric flux rope poles that occurs after the central, horizontal portion of the rope has emerged. To demonstrate this, we examine the evolution of the footpoints of sample magnetic field lines of our flux rope. A movie of this evolution is available as an mpeg file in the electronic edition of the Journal, and Figure 14 shows field line footpoints for four time steps ($t = 30$, 39, 48, 55). At the photosphere each of the field lines we have chosen is associated with a flux surface of the prescribed emerging flux rope; the flux surfaces they are associated with are indicated by the color of the footpoint dots (see the distribution across the flux rope at $t = 55$ in Figure 14: at that time half of the toroidal flux tube has emerged). The large filled circle in each color identifies the footpoint of the last field line we identify to emerge along each flux surface. The magnetic footpoints of our field lines are first seen at $t = 14$, and the

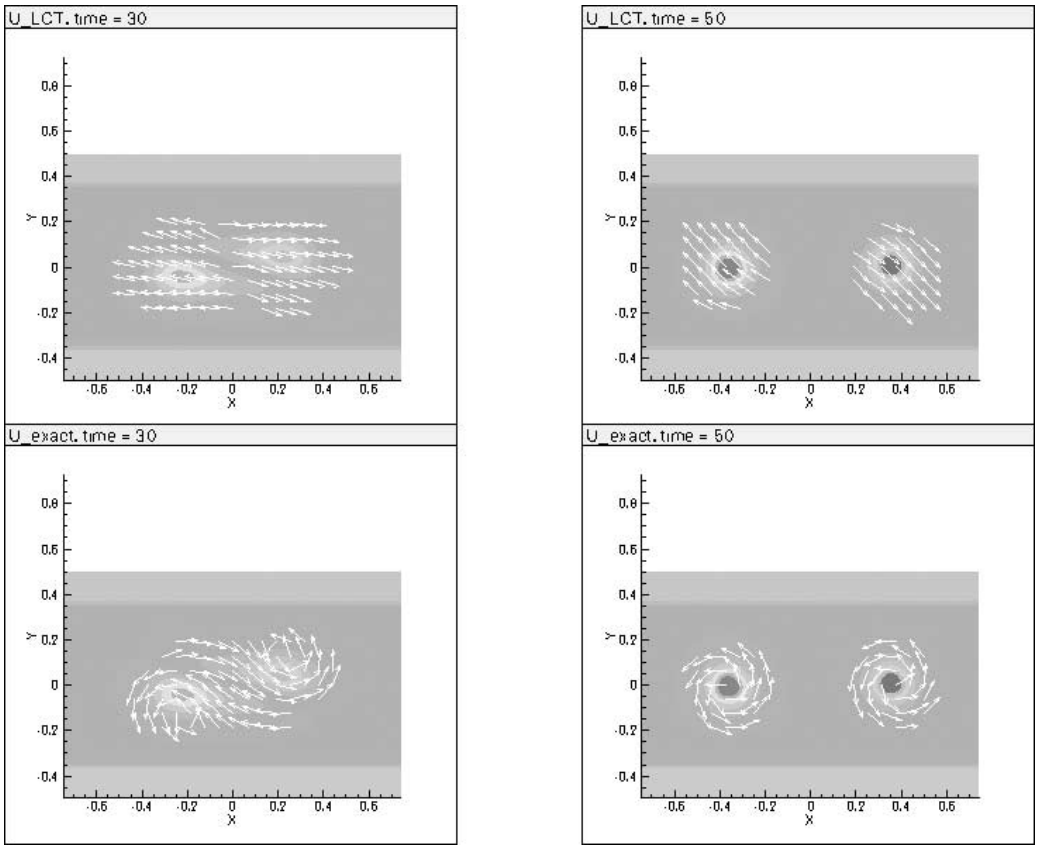

FIG. 12.—Apparent photospheric horizontal velocities, calculated explicitly from the simulation. The velocity vectors of the photospheric footpoints of magnetic field lines ($\boldsymbol{u}_{\rm exact}$; *bottom panels*) and the velocity vectors calculated using LCT analysis of magnetogram time series ($\boldsymbol{u}_{\rm LCT}$; *top panels*) are shown with arrows. Vectors represent direction of velocity tangent to the photosphere: the length of vectors in this figure are uniform and do not represent velocity magnitude. Two times, $t = 30$ and $t = 50$, are shown. [*See the electronic edition of the Journal for a color version of this figure.*]

central axis of the rope emerges at $t = 25$. Distinct apparent vortical motion about the two magnetic poles begins to be visible at $t = 30$, but much of the apparent surface motion of the outer field line footpoints is still lateral, shearing-type motion. We can compare the direction of rotation of the spots in our simulation, that is, counterclockwise, to those of Brown et al. (2003), who found a general trend for such rotation in the northern hemisphere. We have already established that the sign of the magnetic helicity (negative) and direction of sigmoid (backward) are also consistent with observations of the northern hemisphere. The total amount of rotation that might be observed in a sunspot depends on when we decide the sunspot is fully "formed." If we take $t = 39$ as the start time, when most of the apparent lateral motion of footpoints has ceased in favor of vortical motion, we find a maximum rotation of the large, inner pink dot of approximately 100°. If we choose $t = 48$, when the "sunspots" are completely circular and the apparent surface motion is totally vortical, we find a rotation of approximately 50°. Both of these amounts are consistent with the results of Brown et al. (2003). Even if we took the extreme case of choosing $t = 30$ as our beginning time for rotation, we would find a rotation of the large, inner pink dot of no more than 180°, still within the 40°–200° range observed by Brown et al. (2003).

How is this rotation of less than 200° possible, since, as Figure 11 shows, ~1.8 full turns (648°) of helicity emerge in the course of our flux rope evolution? There are two main reasons that observations of sunspot rotation could lead to an underestimate of twist in an emerging flux rope. First of all, a flux rope of the sort that we model will necessarily create two coevolving "sunspots" of opposite magnetic polarity, and each will show rotation to the degree discussed above. Such clearly paired sunspots are not always evident—often the following polarity magnetic pole of an active region is much more diffuse than the leading one—but they have been observed to occur and to exhibit coordinated rotation (Zirin & Tanaka 1973; Ding & Zhang 1982). However, studies such as Brown et al. (2003) are limited by their observing field of view and cannot search for motions in an associated spot, if indeed such a spot could be found. Therefore, the total amount of rotation they find is necessarily limited to individual spots. A proper assessment of the total amount of twist in our flux rope requires adding the contributions from both poles. The second effect that causes us to underestimate the amount of twist in the flux rope is due to the changing orientation of the rope during its emergence. The central portion of the rope is oriented essentially parallel to the photosphere. When we follow footpoints that lie along this horizontal part of the rope, their motion at the photosphere appears to be a lateral, shearing motion such as that associated with flux emergence. A close examination of the initial appearance (not shown in Fig. 14) versus final location of the large, inner pink dot shows that indeed it travels nearly a full 2π relative to the flux rope axis; when doubled to take into account both spots, this yields the approximately 1.8 full turns of helicity in the rope. However, the initial, lateral motion of this footpoint, occurring while the rope axis is oriented parallel to the photosphere, is unlikely to be interpreted as part of a sunspot rotation. Thus a significant part of

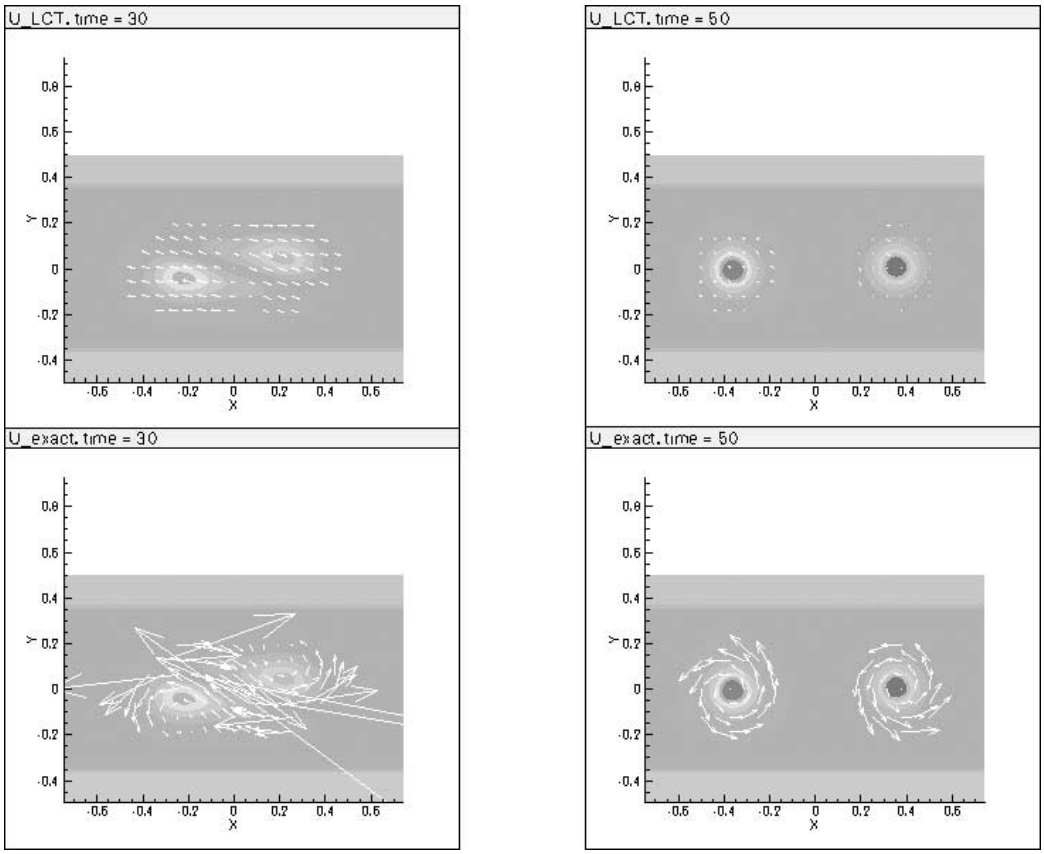

FIG. 13.—Same as Fig. 12, except with velocity vector length representing relative magnitude of velocity. [*See the electronic edition of the Journal for a color version and an mpeg animation of this figure.*]

emerging twist is likely to be missed when considering rotating sunspots.

5. DISCUSSION

Our goal with this paper has been to establish what the observable properties of a magnetic flux rope emerging into a coronal atmosphere are likely to be. Most importantly, our interpretation of the simulation results takes into physical consideration why observed features are visible when and where they are. Despite its topological simplicity, we find that the flux rope model is able to explain a wide range of solar observations, including X-ray sigmoids, sigmoidal, braided, and concave-up features in filaments, and apparent shearing and rotational motions of magnetic field elements.

Our assumption has been that the modeled filament lies in the bottoms of the winds of the flux rope, and that the bald-patch–associated separatrix surface is the site of current sheets and heating. The resulting forms and shapes of (Hα) filaments and their relationship to X-ray sigmoids are then explained self-consistently. Moreover, we have demonstrated that the BPSS is indeed a location of current sheet formation under the dynamic forcing of the system by the kink instability.

Such a kink instability has been dismissed as inconsistent with observations, which have been interpreted to imply a lesser amount of twist being imparted into the photosphere. The observed amount of rotation in a sunspot is significantly less than 2π. Thus there is not enough for the kink instability to arise from twist imparted to coronal loops from photospheric rotational motion of the sunspot (nevertheless, note that Gerrard et al. 2003 performed an MHD simulation that took into account the evolution of the complex field surrounding the sunspot by including both sunspot rotation and observed inflow motions, and found that current sheets indeed formed, unlike the case when only rotational motion was considered). If the twist emerges in the form of a flux rope, however, we have shown that the amount of rotation in a single flux rope leg, which we identify with a sunspot, is consistent with observed rotation of less than 2π. A proper accounting of the total emerging twist in a flux rope requires the inclusion of rotational motions about the other flux rope leg (if such a distinct structure could be found), as well as lateral shearing motions during flux emergence. Thus it is essential to monitor the motions of magnetic elements over as much of their lifetime as possible. For this reason, the emergence of small magnetic bipoles, which have short lifetimes and can be observed from emergence to decay in a few days, may prove to be good candidates for analysis (Mandrini et al. 2004). It is also important to use the highest possible resolution observations so as to best follow the motions of the highly fragmented "real" magnetic field, since, as the analysis in this paper has demonstrated, a smooth or unresolved magnetic distribution can hide a significant amount of rotational motions. The high spatial resolution that will become available with the advent of the *Solar-B* mission will be particularly useful for this.

Recently, doubt was raised about the likelihood of the kink instability playing an important role in coronal dynamics by Leamon et al. (2003), who found that the linear force-free parameter α determined from vector magnetograms for sigmoid regions implied a total twist significantly less than 2π. However, Pevtsov et al. (1994) and Leka (1999) showed that α may vary by an order of magnitude or more across a region, so that the α values determined in the Leamon et al. (2003) study may

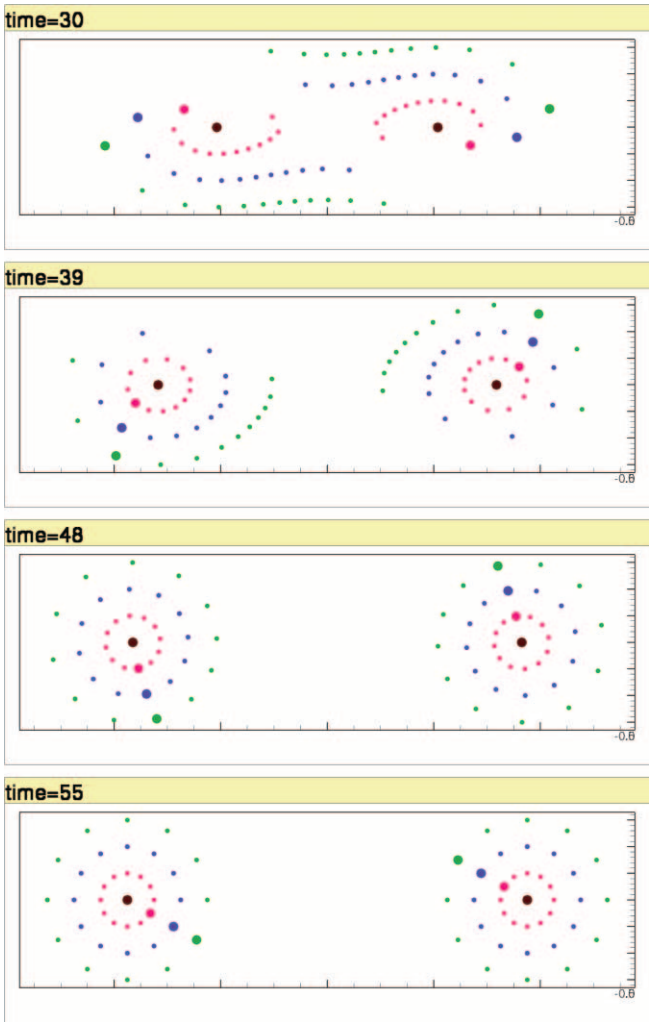

FIG. 14.—Photospheric footpoints of magnetic field lines within the simulated flux rope at four time steps ($t = 30$, 39, 48, 55). Different colors represent the different flux surfaces of the prescribed (subphotospheric) flux rope on which the footpoints of the field lines lie. The large, filled circles are the footpoints of the last emerging field line that we identify on each isocontour. The large dark brown dot is the location of the intersection of the flux rope axis field line with the photosphere. [*This figure is available as an mpeg file in the electronic edition of the Journal.*]

significantly underestimate the amount of twist in more localized regions. In the case of our model, an α determined for the whole region will be smaller than when the overlying potential arcade is excluded, but the difference is not greater than the uncertainties in the analysis. Regardless, in both cases α underestimates the true twist present (K. D. Leka 2004, in preparation). We plan in future to investigate whether the model can be more exactly fitted to observations of photospheric field, and will address the question of how the force-free parameter α would appear for such a revised simulation at that time.

We have commented above that we believe that our simulation of a smooth, kinematic emergence of a flux rope, while likely to be far simpler than the more complex actual transfer of magnetic helicity into the corona, at least qualitatively captures the essential and observable properties of such a transferal. Theory predicts that current sheets will form at the BPSS when the system is dynamically driven on timescales faster than the emergence time, and this indeed happens as the system undergoes a kink instability. However, although our model demonstrates that a kink instability is consistent with observations of photospheric sunspot rotation and sigmoid structures, the kink instability itself is not in general required for them. In the real Sun we would expect current sheets to form at the BPSS under other sorts of dynamic forcings, for example, photospheric footpoint motion acting differently on one end of the BPSS than the other, or expansion upward if loss of filament mass disrupts an equilibrium. Indeed, we would expect heating to occur both in explosive situations like our simulated kink instability and in a more quiescent fashion as the flux rope dynamically emerges and is generally "jiggled" by evolving coronal conditions.

In conclusion, we emphasize that the results of this paper depend upon the presence, growth, and dynamic forcing of a twisted magnetic flux rope in the corona, and not directly on the mechanisms that cause these effects. Whether it is bodily emergence of a flux rope or torsional Alfvén waves that create the twist in the coronal rope, both will ultimately lead to the sort of kink instability we have modeled here. And the kink instability itself is not necessary for the formation of current sheets: it acts as a very efficient driver for current sheet formation along the BPSS, but the BPSS exists prior to the onset of the instability, and a different driver could form current sheets there at any time. The kink instability is simply another consequence of twisted flux emergence. The crucial common element that can explain sigmoid heating events, associated filaments, and observed features of magnetic flux emergence and rotation is the magnetic topology of a magnetic flux rope in the corona.

We thank Graham Barnes, Rekha Jain, K. D. Leka, Dana Longcope, B. C. Low, and Tom Metcalf for helpful discussions. *TRACE* is operated jointly out of Goddard Space Flight Center by scientists from the University of Chicago, Montana State University, LMSAL, and the Harvard-Smithsonian Center for Astrophysics. *SOHO* is a project of international cooperation between ESA and NASA. This material is based on research sponsored by the Air Force Research Laboratory, under agreement number F49620-02-0191. S. G. and Y. F. also acknowledge the support of NASA order number W-19,956. G. F.'s work was supported in part by the DoD MURI grant, "Understanding Magnetic Eruptions on the Sun and their Interplanetary Consequences." C. H. M. and P. D. acknowledge ECOS (France) and SECyT (Argentina) for their cooperative science program (A01U04). Part of C. H. M. and G. F.'s work was done during a visit to NCAR/HAO, funded by the Air Force Research Laboratory.

REFERENCES

Abbett, W., Fisher, G. H., & Fan, Y. 2000, ApJ, 540, 548
———. 2001, ApJ, 546, 1194
Amari, T., Luciani, J. F., Aly, J. J., & Tagger, M. 1996, ApJ, 466, L39
Aulanier, G., & Demoulin, P. 1998, A&A, 329, 1125
Berger, M. A., & Field, G. B. 1984, J. Fluid Mech., 147, 133
Berger, T. E., Lofdahl, M. G., Shine, R. S., & Title, A. M. 1998, ApJ, 495, 973
Brown, D. S., Nightingale, R. W., Alexander, D., Schrijver, C. J., Metcalf, T. R., Shine, R. A., Title, A. M., & Wolfson, C. K. 2003, Sol. Phys., 216, 79
Bungey, T. N., Titov, V. S., & Priest, E. R. 1996, A&A, 308, 233
Canfield, R. C., Hudson, H. S., & Pevtsov, A. A. 2000, IEEE Trans. Plasma Sci., 28, 1786
Chae, J., Wang, H., Qiu, J., Goode, P. R., Strous, L., & Yun, H. S. 2001, ApJ, 560, 476

Chen, J. 1996, J. Geophys. Res., 101, 27499
Cremades, H., & Bothmer, B. 2004, A&A, 422, 307
Demoulin, P., & Berger, M. A. 2003, Sol. Phys., 215, 203
Ding, Y., & Zhang, B. 1982, Sci. China A, 8, 732
Emonet, T., & Moreno-Insertis, F. 1998, ApJ, 492, 804
Fan, Y. 2001, ApJ, 554, L111
Fan, Y., & Gibson, S. 2003, ApJ, 589, L105
———. 2004, ApJ, 609, 1123
Fan, Y., Zweibel, E. G., & Lantz, S. R. 1998, ApJ, 493, 480
Gerrard, C. L., Brown, D. S., Mellor, C., Arber, T. D., & Hood, A. W. 2003, Sol. Phys., 213, 39
Gibson, S., & Low, B. C. 1998, ApJ, 493, 460
———. 2000, J. Geophys. Res., 105, 18187
Gibson, S., et al. 2002, ApJ, 574, 1021
Gilbert, H. R., Holzer, T. E., Low, B. C., & Burkepile, J. T. 2001, ApJ, 549, 1221
Green, L. M., Lopez Fuentes, M. C., Mandrini, C. H., Demoulin, P., van Driel-Gesztelyi, L., & Culhane, J. L. 2002, Sol. Phys., 208, 43
Guo, W. P., & Wu, S. T. 1998, ApJ, 494, 419
Illing, R. M., & Hundhausen, A. J. 1986, J. Geophys. Res., 91, 10951
Kliem, B., Titov, V. S., & Torok, T. 2004, A&A, 413, L23
Kusano, K., Maeshiro, T., Yokoyama, T., & Sakurai, T. 2002, ApJ, 577, 501
Leamon, R. J., Canfield, R. C., Blehm, Z., & Pevtsov, A. A. 2003, ApJ, 596, L255
Leka, K. D. 1999, Sol. Phys., 188, 21
Leka, K. D., Canfield, R. C., McClymont, A. N., & van Driel-Gesztelyi, L. 1996, ApJ, 462, 547
Li, Y., Luhmann, J., Fisher, G., & Welsch, B. 2004, J. Atmos. Sol.-Terr. Phys., submitted
Lites, B. W., & Low, B. C. 1997, Sol. Phys., 174, 91
Lites, B. W., Low, B. C., Martinez-Pillet, V., Seagreaves, P., Skumanich, A., Frank, Z. A., Shine, R. A., & Tsuneta, S. 1995, ApJ, 446, 877
Longcope, D. W. 2004, ApJ, 612, 1181
Longcope, D. W., & Welsch, B. T. 2000, ApJ, 545, 1089
Lopez Fuentes, M. C., Demoulin, P., Mandrini, C. H., & van Driel-Gesztelyi, L. 2000, ApJ, 544, 540
Low, B. C. 1987, ApJ, 323, 358
———. 1994, in Third *SOHO* Workshop: Solar Dynamic Phenomena and Solar Wind Consequences, ed. J. J. Hunt (ESA SP-373; Paris: ESA), 123
Low, B. C. 1996, Sol. Phys., 167, 217
Low, B. C., & Berger, M. 2003, ApJ, 589, 644
Low, B. C., & Hundhausen, J. R. 1995, ApJ, 443, 818
Low, B. C., & Wolfson, R. 1988, ApJ, 324, 574
Manchester, W., Gombosi, T., DeZeeuw, D., & Fan, Y. 2004, ApJ, 610, 588
Mandrini, C. H., Pohjolainen, S., Dasso, S., Green, L. M., Demoulin, P., van Driel-Gesztelyi, L., Copperwheat, C., & Foley, C. 2004, A&A, submitted
Nightingale, R. W., Shine, R. A., Brown, D. S., Wolfson, C. J., Schrijver, K. J., Metcalf, T. R., & Title, A. M. 2002, in COSPAR Colloq. 13, Multi-Wavelength Observations of Coronal Structure and Dynamics, ed. P. C. H. Martens & D. P. Cauffman (Amsterdam: Pergamon), 149
November, L. J., & Simon, G. W. 1988, ApJ, 333, 427
Parker, E. N. 1994, Spontaneous Current Sheets in Magnetic Fields (New York: Oxford Univ. Press)
Pevtsov, A. A. 2002a, in COSPAR Colloq. 13, Multi-Wavelength Observations of Coronal Structure and Dynamics, ed. P. C. H. Martens & D. P. Cauffman (Amsterdam: Pergamon), 125
———. 2002b, Sol. Phys., 207, 111
Pevtsov, A. A., Canfield, R. C., & Metcalf, T. R. 1994, ApJ, 425, L117
Pevtsov, A. A., Maleev, V. M., & Longcope, D. W. 2003, ApJ, 593, 1217
Priest, E. R., Hood, A. W., & Anzer, U. 1989, ApJ, 344, 1010
Roussev, I. I., Forbes, T. G., Gombosi, T. I., Sokolov, I. V., DeZeeuw, D. L., & Birn, J. 2003, ApJ, 588, L45
Rust, D. 1994, Geophys. Res. Lett., 21, 241
Rust, D., & Kumar, A. 1994, Sol. Phys., 155, 69
Shibata, K. 1999, Ap&SS, 264, 129
Strous, L. H., Scharmer, G., Tarbell, T. D., Title, A. M., & Zwaan, C. 1996, A&A, 306, 947
Strous, L. H., & Zwaan, C. 1999, ApJ, 527, 435
Tanaka, K. 1991, Sol. Phys., 136, 133
Titov, V. S., & Demoulin, P. 1999, A&A, 351, 707
Titov, V. S., Galsgaard, K., & Neukirch, T. 2003, ApJ, 582, 1172
Tokman, M., & Bellan, P. M. 2002, ApJ, 567, 1202
Torok, T., & Kliem, B. 2003, A&A, 406, 1043
Torok, T., Kliem, B., & Titov, V. S. 2004, A&A, 413, L27
Welsch, B. T., Fisher, G. H., Abbett, W. P., & Regnier, S. 2004, ApJ, 610, 1148
Wood, B. E., et al. 1999, ApJ, 512, 484
Yu, G. 1973, ApJ, 181, 1003
Zirin, H., & Tanaka, K. 1973, Sol. Phys., 32, 173